論文 / 著書情報
Article / Book Information

Title	3D Finite Element analysis on large-diameter monopiles in dense sand and evaluation of soil degradation under cyclic loading in short-term
Authors	Takaaki Kobayashi, Jaylord Tan Tian, Shintaro Ohno, Toshihiro Sawada, Akihiro Takahashi
Citation	Soils and Foundations, Vol. 66, Issue 5, 101854
Pub. date	2026, 10
DOI	https://doi.org/10.1016/j.sandf.2026.101854
Creative Commons	Information is in the article.

Available online at www.sciencedirect.com

ScienceDirect

Soils and Foundations 66 (2026) 101854

www.elsevier.com/locate/sandf

Technical Paper

3D finite element analysis on large-diameter monopiles in dense sand and evaluation of soil degradation under cyclic loading in short-term

Takaaki Kobayashi [a,*], Jaylord Tan Tian [a], Shintaro Ohno [a], Toshihiro Sawada [b], Akihiro Takahashi [c]

[a] *Civil Engineering Design Division, Kajima Corporation, 3-8, Motoakasaka 1-chome, Minato-ku, Tokyo 107-8477, Japan*
[b] *IMAGEi Consultant, Japan*
[c] *Department of Civil and Environmental Engineering, Institute of Science Tokyo, Japan*

Received 1 August 2025; received in revised form 13 July 2026; accepted 30 July 2026

Abstract

This study investigates the applicability of three-dimensional finite element analysis (3D FEA) for large-diameter monopiles under short-term loading conditions. Centrifuge model tests conducted on saturated, dense Toyoura sand were used to validate the 3D FEA, with a focus on load–displacement response, bending moment distribution, and excess pore water pressure. The results demonstrate that 3D FEA accurately captures the initial loading behavior and key resistance mechanisms, particularly for large-diameter monopiles. Furthermore, the Cyclic Contour Diagram (CCD) concept, a practical approach for predicting degradation due to cyclic loading, was examined. CCD-based degradation factors were compared with stiffness reductions observed in centrifuge model tests, showing reasonable agreement under nearly undrained conditions. Additional FEA incorporating degraded parameters derived from the CCD confirmed the potential of this approach, although limitations remain in accurately reproducing detailed monopile responses. This study highlights the effectiveness of the CCD concept, while emphasizing that its application in practical design requires careful consideration of factors such as load levels, drainage conditions, and the degree of soil mobilization along the monopile. The results provide additional insight into the applicability of CCD-derived degradation characteristics to large-diameter monopiles, highlighting the importance of drainage conditions and pile geometry when interpreting cyclic degradation at the pile level.

Keywords: Wind turbine foundations; Monopile; Centrifuge modelling; Lateral cyclic loading; 3D finite element analysis; Stiffness degradation

1. Introduction

The growing global demand for renewable energy has accelerated the development of offshore wind farms, where monopiles remain the most widely used foundation type, especially in shallow to intermediate water depths. These structures are subjected to complex and dynamic loading conditions, including substantial lateral forces generated by wind and waves. Accurately predicting the behavior of monopiles under such conditions is essential to ensure their structural integrity and long-term performance. As wind turbines continue to increase in size, the corresponding monopiles have also become significantly larger in diameter. However, conventional design methodologies have not kept pace with this trend. For example, the widely

* Corresponding author.
E-mail addresses: t-kobayashi@kajima.com (T. Kobayashi), tantian@-kajima.com (J. Tan Tian), onoshi@kajima.com (S. Ohno), sawada@imageiconsultant.com (T. Sawada), takahashi.a.3a81@m.isct.ac.jp (A. Takahashi).

https://doi.org/10.1016/j.sandf.2026.101854
0038-0806/

adopted API guidelines (API, 2000) rely on soil spring models developed for slender piles, which may not accurately capture the response of large-diameter monopiles. While DNV-GL (DNV-RP-C212, 2021) recommends the use of three-dimensional finite element methods (3D FEM) to assess lateral resistance in such cases, the guidance lacks sufficient detail for practical implementation. This gap highlights the need for more robust and well-defined analytical approaches tailored to the unique characteristics of large-diameter monopiles.

The design methodology recently proposed by the PISA project (Burd et al., 2020; McAdam et al., 2020; Taborda et al., 2020) effectively captures the behavior of large-diameter monopiles and has been gradually gaining acceptance within the industry. This methodology is based on full-scale onshore field tests using monopiles with a diameter of two meters. A common limitation of such field tests is the relatively slow loading rate compared to the dynamic loads induced by wind and wave action in actual offshore environments. This constraint arises from the limited capacity of loading equipment. Under these conditions, the sandy ground is typically assumed to be in a fully drained condition, where no significant excess pore water pressure is generated. Centrifuge modeling tests offer a potential solution to this issue by enabling more realistic loading rates. One of the objectives of this study is to validate the applicability of 3D FEM for large-diameter monopiles under short-term loading conditions through simulation of centrifuge model tests by Takahashi et al. (2022). The target soil condition is dense, saturated sandy ground. The analysis focuses on the first half-cycle of the cyclic loading (the initial one-way loading and the subsequent unloading process).

Another key challenge in the design of monopile foundations is the evaluation of soil degradation under cyclic loading. In recent years, efforts have been made to directly simulate the cyclic loading process in numerical analyses using advanced soil constitutive models (e.g., Pisanò 2019; Liu and Kaynia, 2022; Liu et al., 2022; Chaloulos et al., 2024). However, loads induced by wind and waves during a storm can persist for several to tens of hours, manifesting as irregular wave patterns. Reproducing the entire loading history in numerical simulations is computationally intensive and therefore impractical for engineering applications. As a practical alternative, the Cyclic Contour Diagram (CCD), proposed by Andersen (2015), provides a useful framework for estimating soil degradation due to cyclic loading based on laboratory test data. Nevertheless, there is currently limited empirical evidence supporting the validity of CCD-based approaches for practical design applications. The second objective of this study is to evaluate the applicability of the CCD by comparing its predictions with results obtained from centrifuge model tests by Takahashi et al. (2022).

In the following sections, the setup of the three-dimensional Finite Element Analyses (3D FEA) is first described. An overview of the centrifuge model tests by Takahashi et al. (2022), which form the basis for the numerical simulations, is then presented. Subsequently, the results of the 3D FEA are compared with those obtained from the centrifuge model tests in terms of load–displacement response, bending moment distribution along the monopile, and pore water pressure in the surrounding soil. Finally, the CCD concept is examined using both the results of the laboratory test and the centrifuge model tests.

The numerical framework and constitutive models employed in this study are not newly developed but represent widely used, practice-oriented approaches. The objective of this study is therefore not to propose a new constitutive model or finite element formulation, but to evaluate how CCD-derived degradation characteristics can be interpreted at the monopile level through three-dimensional finite element analyses. Particular attention is given to the influence of drainage conditions and monopile geometry on the applicability of CCD-based degradation assessment. Through this approach, the study aims to provide practical insight into the interpretation of laboratory-derived cyclic degradation characteristics for large-diameter monopile foundations.

2. Overview of 3D FEA

2.1. Centrifuge model tests

A series of centrifuge model tests conducted by Takahashi et al. (2022) is briefly reviewed. The test results are utilized to inform the three-dimensional Finite Element analysis (3D FEA) and to examine the degradation effects due to cyclic loading, as discussed in later sections. Fig. 1 presents schematic views of the test configuration at prototype scale under a centrifugal acceleration of 50G. Three monopile configurations were examined, with outer diameters D of 2.0 m and 1.25 m and embedment lengths L of 7.5 m and 10 m. The distance from the ground surface to the loading point was kept constant at 7.05 m for all monopiles. As a result, the tested monopiles cover slenderness ratios L/D of 3.75, 5, and 8. The monopile with an outer diameter of two meters is smaller than those recently adopted in practice; however, it was selected due to limitations of the testing facility. The model ground consisted of saturated Toyoura sand with a relative density of approximately 80%. Its mechanical properties are summarized in Table 1. The ground was prepared by air pluviation in a dry state and subsequently saturated using de-aerated pore fluid under vacuum pressure. The model monopile was placed in the container prior to sand deposition, meaning that the ground was not disturbed by pile installation. The model monopile was a closed-ended hollow tube, preventing sand from entering the interior. A brass cap was installed at the pile tip to simulate the self-weight of the sand that would otherwise occupy the pile.

Two-way lateral loads were applied to the monopile in a displacement-controlled manner following the sequence

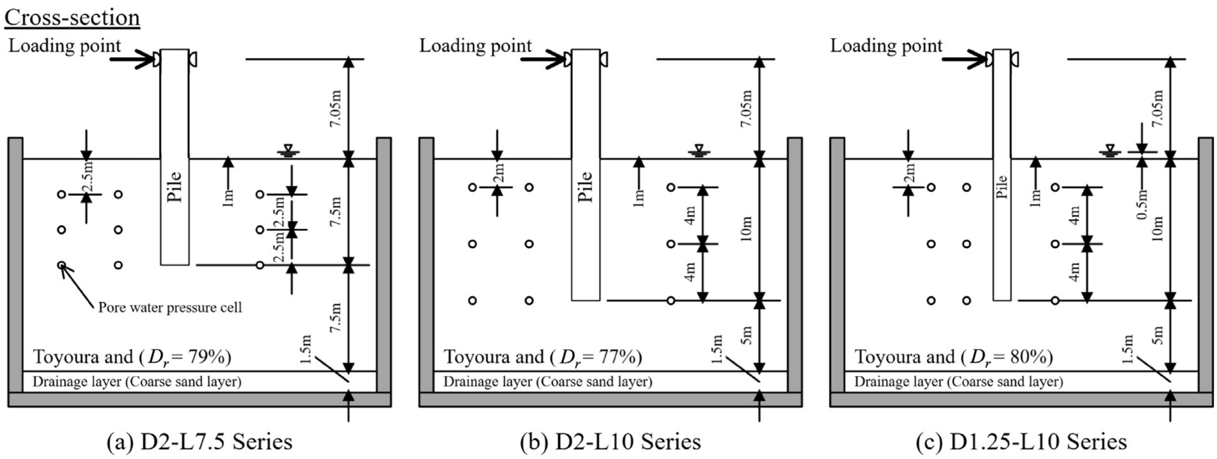

Fig. 1. Model configurations at prototype scale (After Takahashi et al., 2022).

Table 1
Mechanical properties of Toyoura sand (Takahashi et al., 2022).

Property		Unit	Value
Specific gravity	G_s	–	2.655
Maximum void ratio	e_{max}	–	0.916
Minimum void ratio	e_{min}	–	0.593
Mean diameter	d_{50}	mm	0.19
Coefficient of permeability at Dr = 80%	k	m/s	3.87×10^{-5}

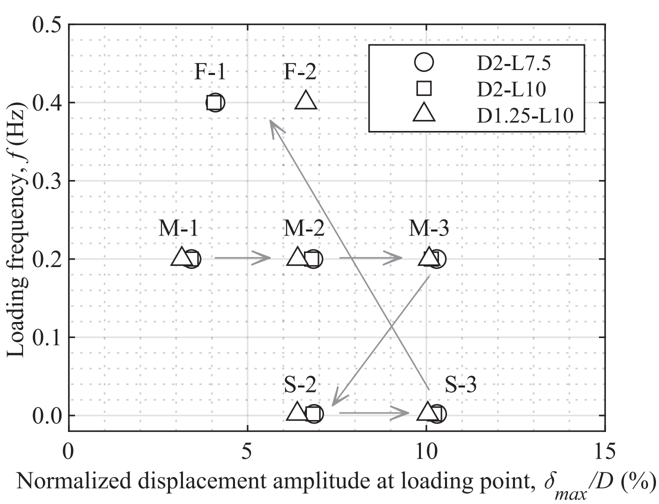

Fig. 2. Loading conditions and sequences in centrifuge model tests (After Takahashi et al., 2022).

shown in Fig. 2. The loading frequency and amplitude were varied to represent different loading conditions. The drainage response in the centrifuge tests was controlled by adjusting the pore fluid viscosity using methylcellulose (Metolose), allowing conditions ranging from fully drained to nearly undrained to be investigated, depending on the loading rate. Measurements included lateral load, displacement and strain of the monopile, as well as pore water pressure in the surrounding soil. Representative records are reported in Takahashi et al. (2022) and are not reproduced here for brevity.

While Takahashi et al. (2022) primarily focused on loadings S-2 and M−2, the present 3D FEA targets loadings S-3 and M−3 to simulate larger displacements. Note that the influence of prior loading stages on the experimental response cannot be completely excluded. However, loading stage M−3 corresponds to the third of the seven loading stages, and the preceding two loadings were conducted at lower load levels, such that the effect of prior loading is considered relatively small. For this reason, M−3 was selected as the main target for comparison with the FE simulations, in which the effects of prior loading were not explicitly considered. Loadings F-1 and F-2 were excluded due to slightly inconsistent behavior, possibly caused by ground densification from earlier loading sequences. First, the horizontal load–displacement response for loading S-3 is shown for the three monopile types in Fig. 3. A total of three cycles of lateral loading were applied at a frequency of 0.002 Hz (prototype scale). The maximum lateral displacements of the monopile were approximately 0.10D at the loading point and 0.04D at the mudline. All three monopiles exhibited similar hysteresis loops across the three cycles, indicating no significant degradation of the model ground. No progressive accumulation of pore water pressure was observed (See Takahashi et al., 2022), suggesting fully drained conditions under this slow loading rate.

Next, Fig. 4 shows the horizontal load–displacement response for loading M−3. Here, 20 cycles of lateral loading were applied at a frequency of 0.2 Hz (prototype scale). The peak loads in the first cycle of M−3 were comparable to those in S-3. This may be attributed to the limited accumulation of excess pore pressure at this stage, such that the initial soil skeleton stiffness remains the dominant factor governing the pile response. However, in the subsequent cycles, the peak loads decreased significantly, with the 20th cycle reaching only approximately 50% of the initial peak load. This reduction is generally attributed to the accumulation of excess pore water pressure, which resulted in a degradation of ground stiffness. These results suggest that the model ground was in an undrained or partially

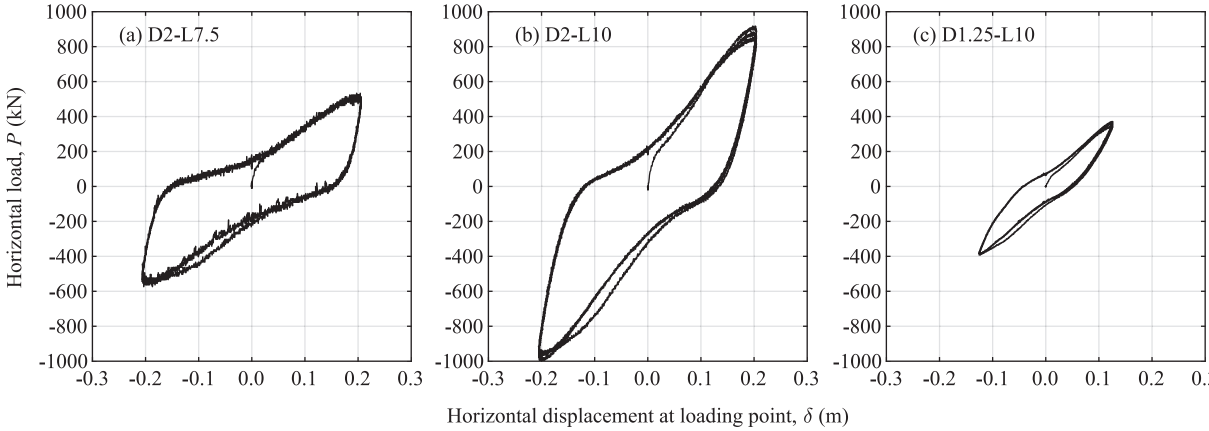

Fig. 3. Horizontal load–displacement response at the loading point for model test S-3 under cyclic loading at a frequency of 0.002 Hz.

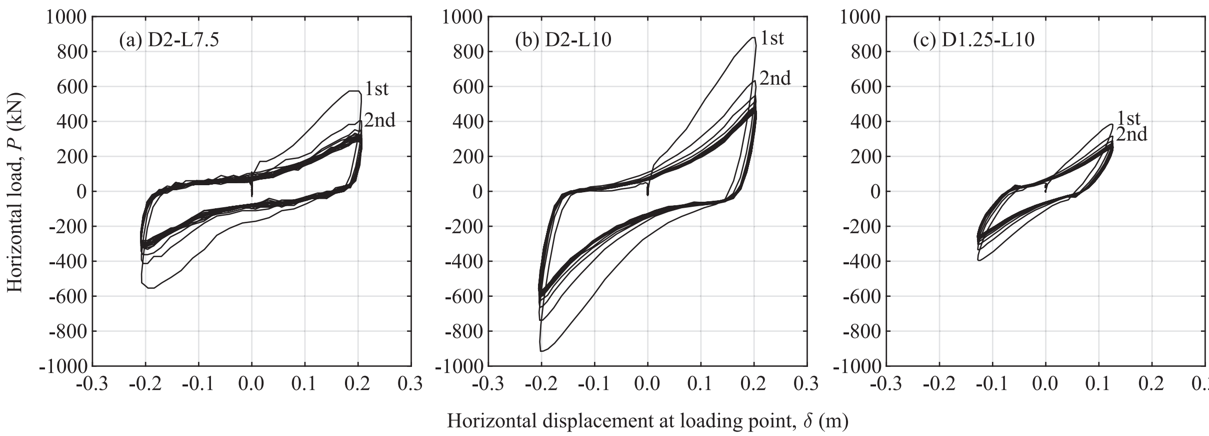

Fig. 4. Horizontal load–displacement response at the loading point for model test M−3 under cyclic loading at a frequency of 0.2 Hz.

drained condition under the faster loading rate. A more detailed discussion of drainage conditions is provided in Section 4.3. It should be noted that the degradation observed in the load–displacement response reflects the integrated effect of stiffness and strength changes over the entire soil domain surrounding the monopile, rather than the excess pore pressure response at a specific depth. Although Takahashi et al. (2022) reported that the excess pore pressure ratio measured at $z = 1D$ remained approximately constant after the initial loading cycles, continued pore pressure accumulation at greater depths may contribute to a reduction in the overall lateral resistance of the pile. This effect is considered particularly important for large-diameter monopiles, where deeper soil layers and toe resistance contribute significantly to the global pile response.

2.2. Constitutive model

The Hardening Soil model with small-strain stiffness (HSS model) was selected to represent the soil behavior in the 3D FEA. A detailed description of the HSS model is provided by Schanz et al. (1999) and Bentley Systems (2023b). The HSS model extends the conventional Hardening Soil (HS) model by incorporating small-strain stiffness characteristics, enabling more accurate predictions of soil deformation (Benz, 2007). It includes multiple stiffness moduli, such as secant, tangent, and unloading/reloading, and accounts for stress-dependent stiffness. The model assumes a hyperbolic stress–strain relationship during primary loading in a standard drained triaxial test. An elasto-plastic formulation is adopted, featuring isotropic hardening of two yield surfaces: a cone and a cap. Key parameters are derived from standard laboratory tests, including oedometer and triaxial compression tests. The HSS model has been successfully applied in simulations of offshore monopile foundations (e.g., Brinkgreve et al., 2020; Ishii et al., 2024). Furthermore, its performance has been evaluated through comparisons with other constitutive models, as discussed by Jostad et al. (2020) and Kaltekis et al. (2023).

Table 2 presents the parameters of the HSS model for Toyoura sand with a relative density of 80%, derived from a series of laboratory tests. Initially, the small-strain shear modulus G_0^{ref}, the threshold shear strain $\gamma_{0.7}$, and the stress-level dependency coefficient m were determined. Fig. 5

Table 2
Parameters of HSS model for model ground.

Parameter		Unit	Value
Saturated unit weight	γ_{sat}	kN/m^3	19.93
Secant stiffness in drained triaxial test	E_{50}^{ref}	kN/m^2	19.0×10^3
Tangent stiffness for oedometer	E_{oed}^{ref}	kN/m^2	19.0×10^3
Unloading/reloading stiffness	E_{ur}^{ref}	kN/m^2	57.0×10^3
Poisson's ratio for unloading/reloading	υ_{ur}	–	0.300
Stress-level dependency of stiffness	m	–	0.68
Reference stress for stiffnesses	p^{ref}	kN/m^2	50.0
Reference shear modulus at small strain	G_0^{ref}	kN/m^2	5.000×10^4
Threshold shear strain at 70% of G_0	$\gamma_{0.7}$	–	0.15×10^{-3}
(Effective) cohesion	c'_{ref}	kN/m^2	0.0
(Effective) angle of internal friction	φ'	degree	40.0
Angle of dilatancy	ψ	degree	10.0

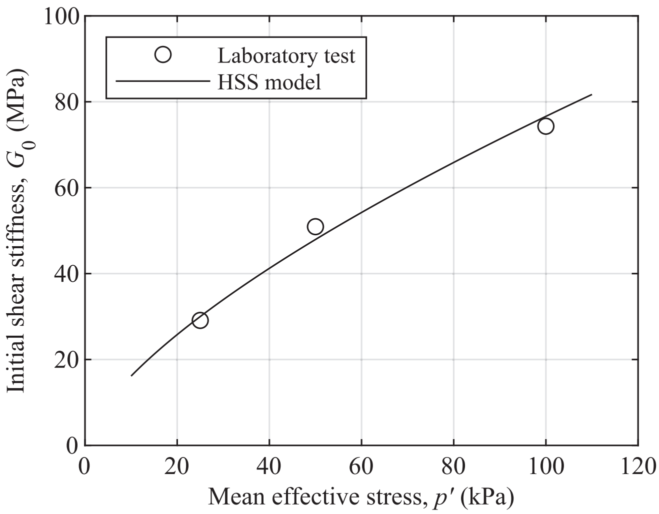

Fig. 5. Stress dependency of initial shear stiffness G_0.

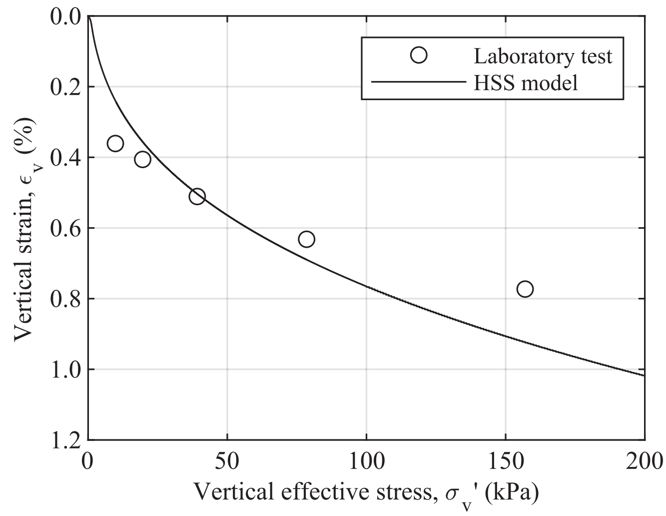

Fig. 6. Simulation of oedometer test.

illustrates the shear modulus G_0 at three different confining pressures, obtained from cyclic triaxial tests (JGS, 2017a). The black solid line represents a fitted curve based on the HSS model, which follows a nonlinear power-law function governed by the coefficient m. An emphasis is placed on the confining pressure range below 150 kPa, as this range corresponds to the depth of the model ground (15 m). Under lateral loading, a slender monopile induces deformation primarily in the shallow ground. In contrast, a large-diameter monopile exhibits stiffer behavior, with deformation extending to the toe due to rotational effects. Therefore, while accurate modeling of the shallow ground is critical, the contribution of deeper layers cannot be disregarded.

Subsequently, the tangent stiffness for oedometer loading, E_{oed}^{ref}, was determined. Fig. 6 shows the results of the oedometer test (JGS, 2015) alongside a simulation conducted using the SOILTEST tool in PLAXIS 3D (Bentley Systems, 2023a). The parameter E_{oed}^{ref}, was calibrated to match the laboratory data, represented by hollow circles. Following the recommendations for the HSS model (Bentley Systems, 2023b), the remaining stiffness parameters were estimated as follows: the secant stiffness in drained triaxial tests $E_{50} = E_{oed}$, and the unloading/reloading stiffness $E_{ur} = 3 \times E_{oed}$.

Finally, simulations of two different undrained shear tests were performed to calibrate the remaining parameters related to strength and dilatancy. Although drained triaxial tests are generally preferred for calibrating HSS model parameters, undrained shear tests were employed due to limitations in the available laboratory data. Fig. 7 presents the simulation result of the undrained direct simple shear test, (a) shear stress vs shear strain and (b) stress path. The corresponding laboratory data were obtained from torsional shear tests on hollow cylindrical specimens (JGS, 2018), which serve as an alternative method for applying simple shear. The black dotted line indicates the monotonic shear test, while the gray solid lines represent the initial cycles of four different cyclic shear tests. Particular attention is given to the shear strain range below 6%, as this range is expected to be most relevant in the model tests. Additionally, a simulation of the undrained triaxial compression test was conducted to further refine the model parameters (Fig. 8(a) and (b)). Only results from

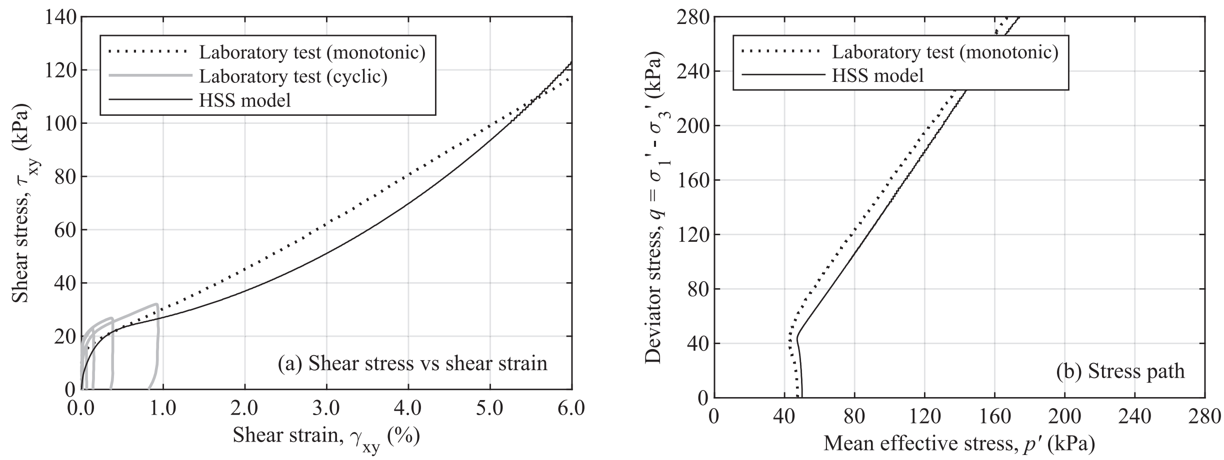

Fig. 7. Simulation of undrained direct simple shear test.

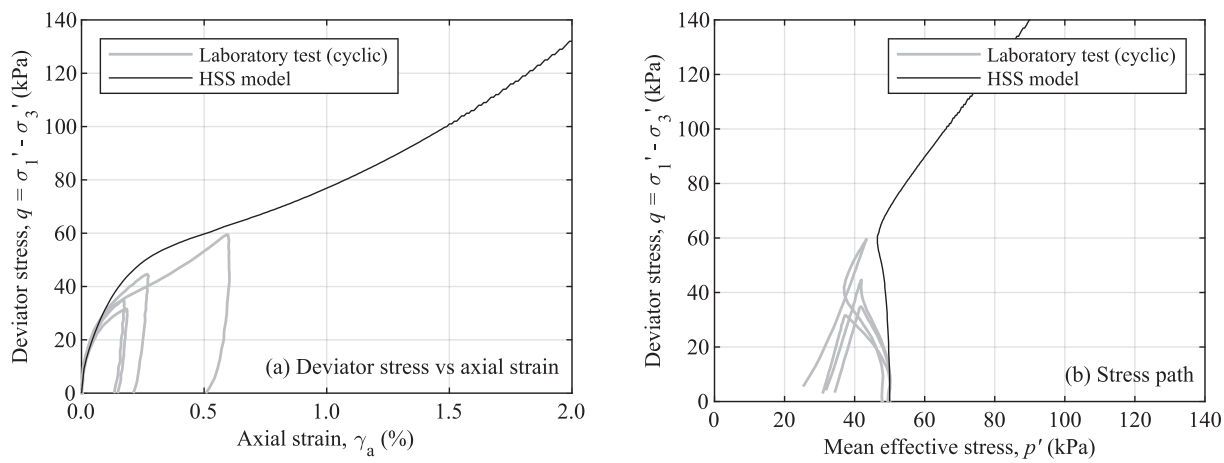

Fig. 8. Simulation of undrained tri-axial compression test.

four cyclic shear tests (JGS, 2017b) were available, shown as gray solid lines. A comparison between Figs. 7 and 8 indicates that the simulation slightly underestimates the shear stress in the torsional shear test, while it overestimates the shear stress in the triaxial compression test. This discrepancy arises because the HSS model does not account for differences in stress paths. For instance, Jostad et al. (2020) identified three distinct parameter sets for triaxial compression, triaxial extension, and direct simple shear for Dogger Bank sand. If anisotropy is significant, a more advanced constitutive model would be preferable. However, for Toyoura sand in this study, the observed differences are within acceptable limits, and the HSS model is considered adequate for capturing the overall behavior of the model ground.

2.3. 3D FE model

The 3D FEA was performed using PLAXIS 3D (version 2024.1; Bentley Systems, 2023a). The modeling approach for the monopile, surrounding soil, and their interfaces follows the methodology adopted in PLAXIS Monopile Designer (Bentley Systems, 2023c). The FE model domain was defined to be consistent with the dimensions of the

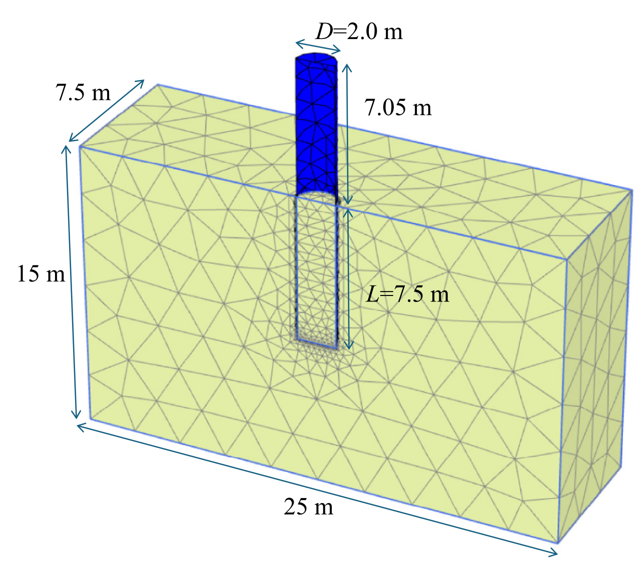

Fig. 9. Three-dimensional Finite Element model for (a) D2-L7.5.

rigid soil container used in the centrifuge tests. Owing to symmetry, only half of the domain was modeled, as illustrated in Fig. 9. The numerical models consisted of approximately 4000, 10-node tetrahedral elements. For the monopiles, 6-node triangle plate elements with the linear elastic model were used, and their properties are summarized in Table 3. It should be noted that the monopile was modeled as an open-ended pile with internal soil, whereas a closed-ended pile with a brass-made cap at the tip to replicate the weight of the internal soil was used in the model tests. In the initial phase of the simulation, the soil domain was generated, and the initial stress distribution was computed. In the subsequent phase, the monopile was introduced using the "wished-in-place" method, which is consistent with the experimental setup where the model monopile was installed without disturbing the surrounding soil. During the loading phase, the "Consolidation" calculation type was employed, which performs a fully coupled deformation–flow analysis. This option solves the mechanical equilibrium of the soil skeleton together with the transient groundwater flow equation (u–p formulation), thereby accounting for excess pore water pressure generation and dissipation during loading. Lateral displacement was applied at the loading point of the monopile at loading rates corresponding to S-3 (0.002 Hz) and M−3 (0.2 Hz) in the model tests. Interface elements were introduced between the soil and the monopile, with an interface reduction factor $R_{inter} = 0.6$. In this setting, the interface shear strength is modeled as a fraction of the adjacent soil strength, with $\tan \varphi'_{int} = R_{inter} \cdot \tan \varphi'_{soil}$; here, φ'_{int} and φ'_{soil} denote the interface and soil friction angles. Consistent with this, the elastic interface stiffness is also scaled internally relative to R_{inter}. We selected R_{inter} to represent a realistic interface roughness/friction angle consistent with the centrifuge conditions, rather than to account for installation effects. The choice of R_{inter} can influence the computed response; values around 0.6 are also commonly adopted in the literature. For example, Ishii et al. (2024) reproduced field and model test results for monopiles using $R_{inter} = 0.6$ despite variations in scale and installation method.

3. Results of 3D FEA

3.1. Load-displacement response

The 3D FEA was evaluated against the model tests in terms of load–displacement response, bending moment distribution along the monopiles, and excess pore water pressure in the surrounding ground. Fig. 10 presents the load–displacement response at the loading point for loading case S-3 (0.002 Hz). As demonstrated in Takahashi et al. (2022), the displacement profile along the pile axis for large-diameter monopiles can be well approximated by theoretical solutions assuming a rigid pile. In this context, the load–displacement response at the loading point is considered a representative indicator of monopile behavior. The gray and black solid lines represent the results from the model tests and the 3D FEA, respectively. The curves correspond to the first half cycle, i.e., the initial loading followed by unloading. The overall response is well captured for all three monopiles with different slenderness ratios (L/D = 3.75, 5 and 8). Similarly, Fig. 11 shows the load–displacement response for loading case M−3 (0.2 Hz) for the first half cycle. Despite the faster loading rate in M−3, the 3D FEA demonstrates good agreement with the experimental results. In both S-3 and M−3, the 3D FEA tends to slightly underestimate the initial stiffness observed in the model tests. Additionally, the peak loads are overestimated by approximately 10–15% for case (b) D2-L10 in both loading cases.

Beyond the initial loading and unloading, the FEA encounters limitations in capturing the load–displacement behavior. In the model tests, the monopiles exhibited softening behavior (i.e., reduced stiffness) after the lateral load became negative (see the bottom right quadrant in Figs. 3 and 4), which is not reproduced in the FE simulations. This discrepancy is primarily attributed to the limitations of the constitutive model in representing the cyclic behavior of sand. As noted by Jostad et al. (2020), the HSS model is not capable of simulating the softening response of soils under cyclic loading. Another contributing factor may be the limitations of the FE framework in modeling complex geometric phenomena around the monopile, such as gap formation. Several studies and research initiatives have explicitly incorporated ratcheting behavior into numerical models and design methodologies, recognizing its significance in understanding the cyclic response of monopiles (e.g., Tantivangphaisal et al., 2024; Byrne et al., 2025; Pisanò et al., 2025). However, due to the complexity and computational cost, such modeling approaches remain challenging for practical design applications and are therefore beyond the scope of this study.

3.2. Bending moment and soil deformation

Figs. 12 and 13 present the bending moment distribution along the embedded portion of the monopile for loading cases S-3 and M−3, respectively. The results from the 3D FEA, shown as hollow markers, are compared with those from the model tests, represented by black solid lines, at the point of maximum lateral displacement. The comparison demonstrates good agreement across different slenderness ratios L/D, indicating that the adopted modeling methodology is appropriate. It is noteworthy that the FEA yields non-zero bending moments at the pile base in

Table 3
Parameters of elastic model for monopiles.

Parameter		Unit	Value
Young's modulus	E	kN/m^2	193.0×10^6
Poisson's ratio for unloading/reloading	v	–	0.300
Monopile wall thickness	t	m	0.025

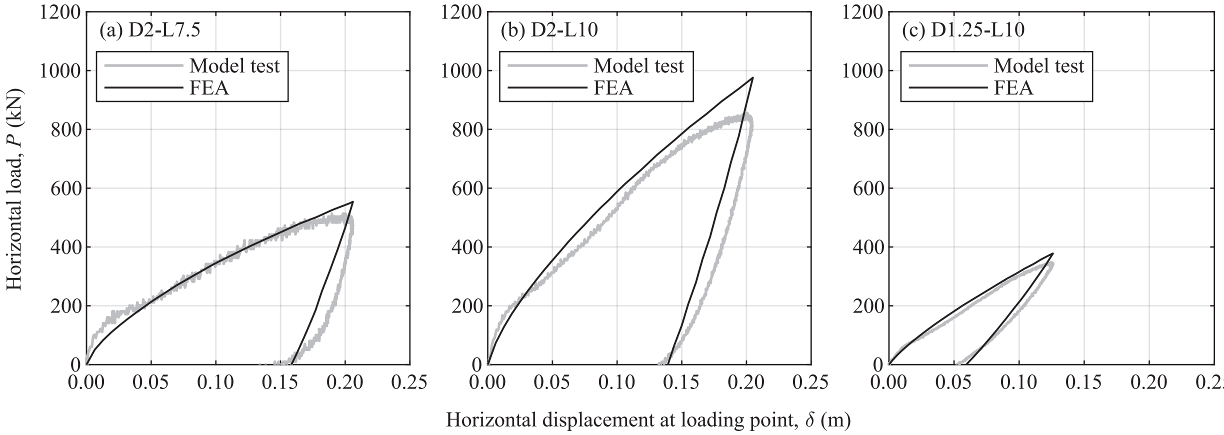

Fig. 10. Simulation of model test S-3 (0.002 Hz): Horizontal load–displacement response at loading point.

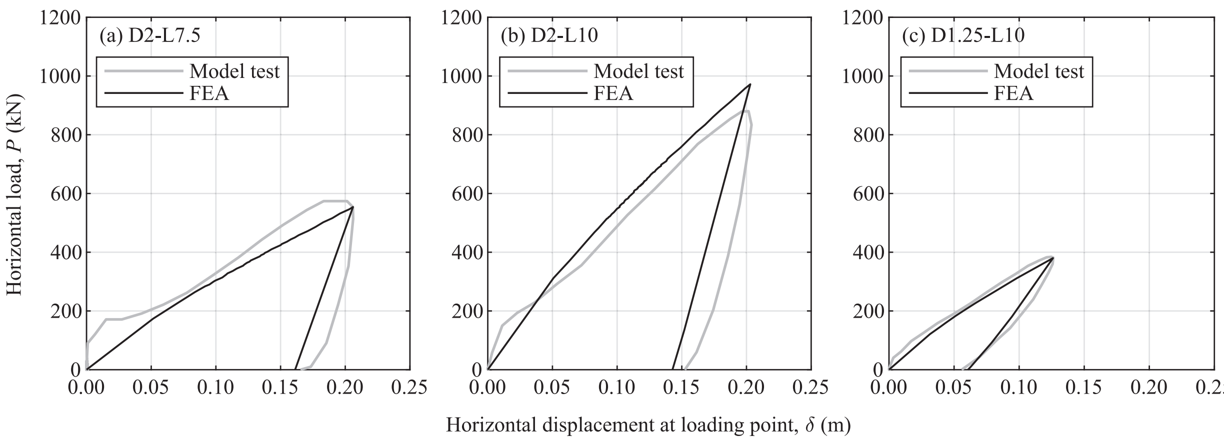

Fig. 11. Simulation of model test M−3 (0.2 Hz): Horizontal load–displacement response at loading point.

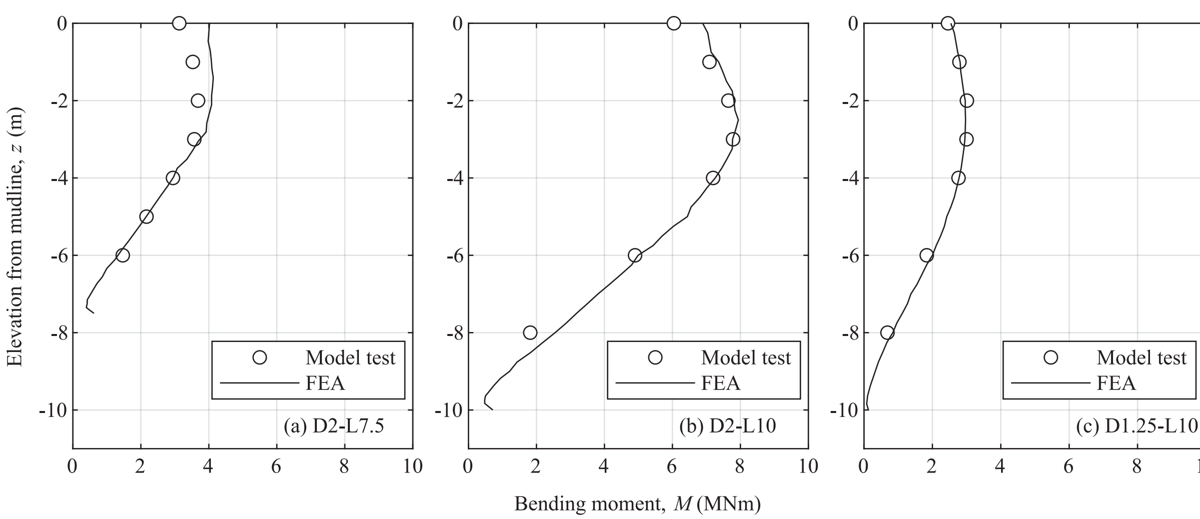

Fig. 12. Simulation of model test S-3 (0.002 Hz): Bending moment along the monopile at the maximum lateral displacement.

the cases of large-diameter monopiles, specifically (a) D2-L7.5 and (b) D2-L10. This suggests the presence of base resistance, a characteristic feature of large-diameter monopiles. Such behavior was also predicted by the analytical solution proposed by Takahashi et al. (2022). Base resistance, along with rotational resistance along the pile shaft, constitutes a key load-resisting mechanism for large-diameter monopiles. These mechanisms are central to the

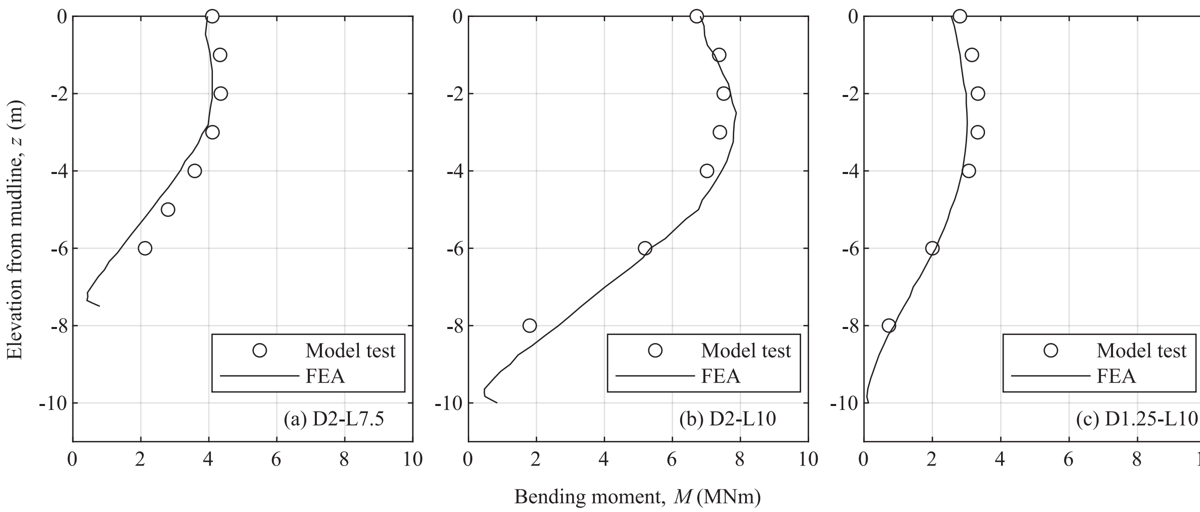

Fig. 13. Simulation of model test M−3 (0.2 Hz): Bending moment along the monopile at the maximum lateral displacement.

PISA design methodology (Burd et al. 2020), which emphasizes the importance of capturing both shaft and toe interactions in monopile design.

The base resistance mechanism is also illustrated by the distribution of deviatoric strain obtained from the 3D FEA as shown in Fig. 14. In all cases, deviatoric strain is concentrated around the pile shaft near the ground surface, both on the loading side and the opposite side of the pile, indicating localized soil deformation associated with lateral pile movement. In the large-diameter monopiles, namely (a) D2–L7.5 and (b) D2–*L*10, additional strain accumulation is observed around the pile toe. This observation is consistent with the non-zero bending moments at the pile base shown in Figs. 12 and 13 and provides further evidence that toe resistance contributes to the overall lateral resistance of the monopile. In contrast, the smaller-diameter monopile (c) D1.25–*L*10 shows limited strain accumulation near the pile toe, suggesting a less significant contribution from base resistance. Furthermore, deviatoric strains exceeding approximately 5% are confined to a relatively limited region adjacent to the pile in cases (a) and (b), whereas such strain levels are not observed in case (c). These results are consistent with the interpretation that the deformation mechanism of large-diameter monopiles involves the combined contribution of shaft and toe resistance, whereas the response of the smaller-diameter monopile is governed primarily by shaft resistance.

3.3. Excess pore water pressure

Fig. 15 illustrates the distribution of excess pore water pressure obtained from the FEA when the monopile reaches its maximum lateral displacement during the initial loading cycle. The results are presented only for loading case M−3, as no significant accumulation of excess pore water pressure was observed in case S-3. Positive excess pore water pressure is observed at mid-depth on the loading side of the monopile. In contrast, negative excess pore water pressure develops behind the monopile due to expansive deformation of the ground. An opposite pattern is evi-

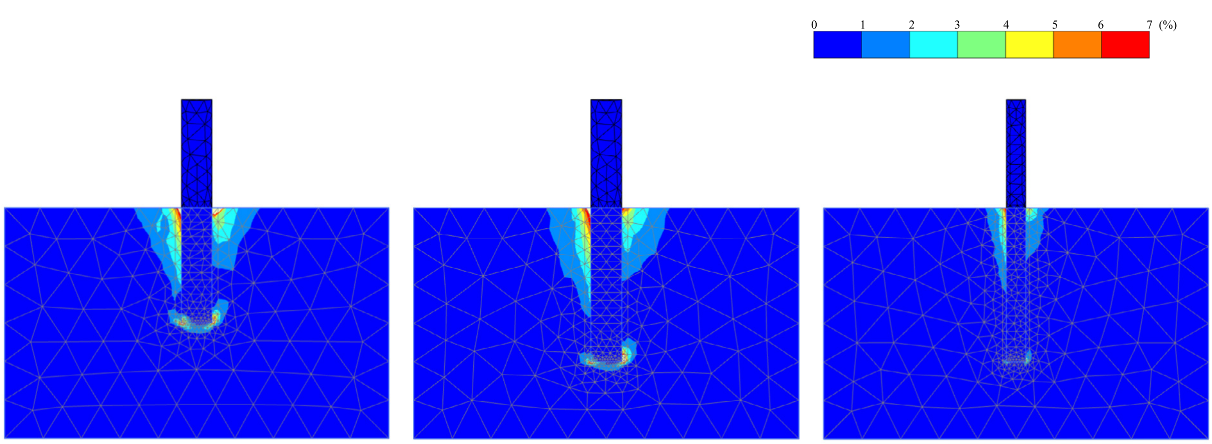

Fig. 14. Simulation of model test M−3 (0.2 Hz): Distribution of deviatoric strain at the maximum lateral displacement.

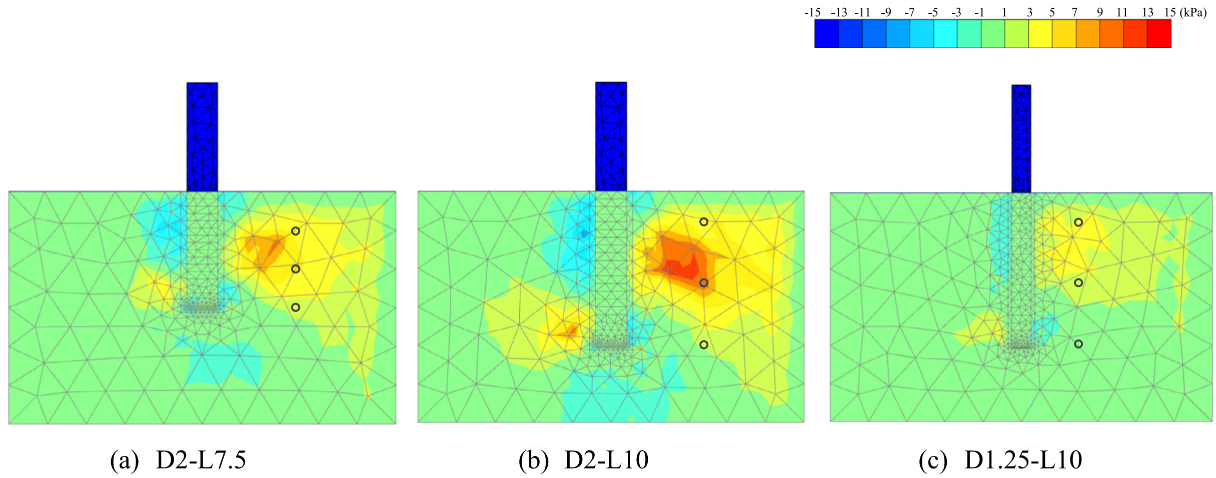

Fig. 15. Simulation of model test M−3 (0.2 Hz): Distribution of excess pore water pressure at the maximum lateral displacement.

dent near the pile toe, particularly in cases (a) D2-L7.5 and (b) D2-*L*10, where negative pressure appears on the loading side and positive pressure behind the pile. This phenomenon is attributed to the "toe-kick" effect, a characteristic behavior of large-diameter monopiles.

Fig. 16 shows a quantitative comparison of excess pore water pressure between the FE analyses and the model tests at the pore water pressure transducer locations. The locations of the sensors are indicated by hollow circles in Fig. 15. The FEA results are represented by the maximum value obtained during the first half of the loading cycle. For comparison, the laboratory data are presented as a range representing the maximum excess pore water pressure recorded over the 1st to 20th loading cycles. The left end of this range corresponds to the peak value within the first cycle and is therefore used as the basis for comparison with the FEA results. The dotted line indicates the initial vertical effective stress, serving as a reference for the potential onset of liquefaction. The results indicate that the model ground remained well below the liquefaction threshold, except at the shallowest part. While the FEA provides a reasonable evaluation, it slightly underestimates the excess pore water pressure at the shallowest measurement points. Overall, the HSS model demonstrates good predictive capability for the behavior of dense sand when parameters are carefully calibrated. The 3D FEA effectively captures the response of monopiles with varying slenderness ratios ($L/D = 3.75$, 5 and 8) under various loading rates.

4. Stiffness degradation under cyclic loading

4.1. Overview

The evaluation of degradation caused by cyclic lateral loading is a critical aspect of practical foundation design, particularly for offshore structures subjected to repeated environmental forces. The previous section focused on the 3D FEA under initial loading, followed by unloading. As noted earlier, simulating the full sequence of cyclic load-

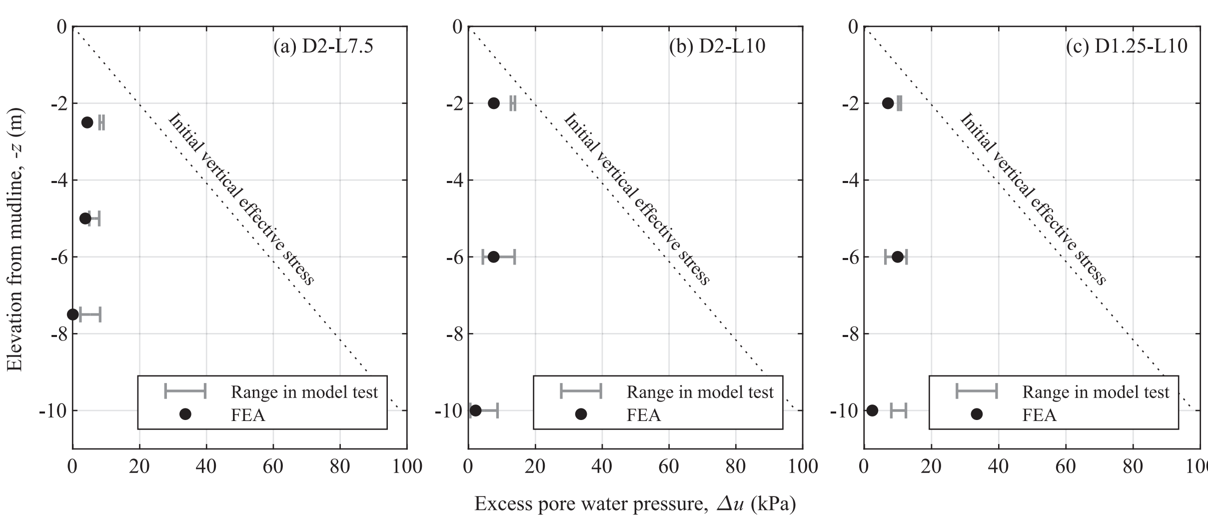

Fig. 16. Simulation of model test M−3 (0.2 Hz): Profile of excess pore water pressure near the monopile.

ing during an entire storm event remains a significant challenge in geotechnical modeling. As a practical alternative, the Cyclic Contour Diagram (CCD), proposed by Andersen (2015), offers a useful framework for estimating the degree of soil degradation under cyclic loading. The CCD concept offers several advantages over conventional approaches:

- Degradation is assessed based on laboratory test results, allowing direct incorporation of material-specific characteristics.
- The extent of degradation is dependent on the intensity of the cyclic loading, represented by the number of load cycles, N.
- Stress–strain curves for the degraded material can be derived and subsequently used in finite element (FE) analyses.

In this section, the CCD concept is examined using both model test and laboratory test results. First, a CCD is constructed based on laboratory test results for Toyoura sand. From this diagram, the degree of degradation and the corresponding degraded stress–strain curves are interpreted. Next, the extent of degradation observed in the model tests is quantified and compared with the evaluation from the CCD. Finally, the HSS model is re-calibrated using the degraded stress–strain curves, with the aim of predicting monopile behavior under cyclic loading conditions as observed in the model tests.

4.2. Cyclic contour diagram and degradation factor

The first step involves constructing the CCD using results from undrained cyclic shear tests. While the original CCD framework (Andersen, 2015) incorporates triaxial compression, triaxial extension, and direct simple shear (DSS) tests, this study only utilizes undrained hollow cylinder cyclic torsional shear tests as an alternative to DSS. Although this represents a simplification relative to field conditions, considering the loading conditions in the element tests and the centrifuge tests (fully reversed cyclic loading), we assumed the average shear stress τ_a to be zero and considered only the cyclic component τ_{cyc}. Fig. 17 presents the CCD for Toyoura sand with a relative density of 80%, where the double amplitude shear strain γ_{DA} is plotted against the number of loading cycles N and the cyclic shear stress ratio CSR (=τ_{cyc}/σ'_c, where σ'_c is the isotropic confining pressure). Similar plots are commonly used in liquefaction studies for earthquake loading, which typically involve tens of cycles. However, offshore foundations may experience hundreds to thousands of cycles due to wave and wind loading (LeBlanc et al., 2010a). The shaded region in Fig. 17 indicates the range of CSR values tested in the laboratory. For the test data indicated by hollow markers, fitting curves were generated at 1% intervals of shear strain. These curves are defined by a power function of the form $y = ax^b$, where a and b are constants, and are

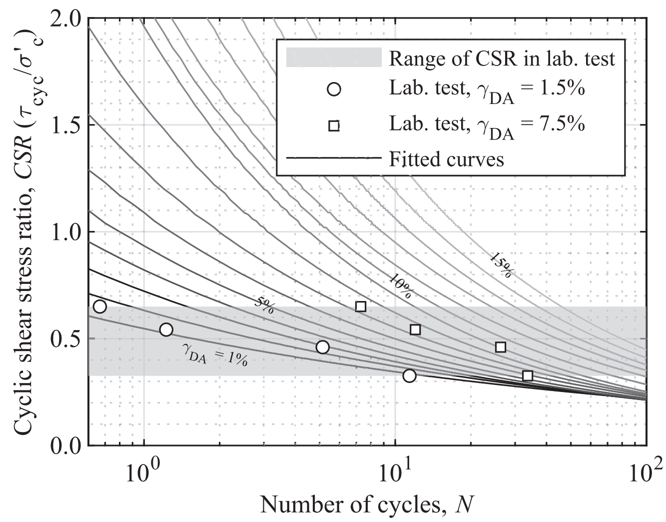

Fig. 17. Cyclic contour diagram obtained by undrained hollow cylinder cyclic torsional shear tests for Toyoura sand with a relative density of 80%.

extrapolated beyond the tested range. It should be noted that such extrapolation may reduce accuracy, and additional testing is recommended for improved reliability.

The next step involves deriving stress–strain curves that reflect the degradation effects captured in the CCD. These curves are constructed by identifying the intersections of shear strain and CSR at specific values of N. A similar process was also presented in Erdrich et al. (2010). Fig. 18 shows the resulting curves for various numbers of load cycles, where γ_{DA} is converted to single amplitude shear strain γ_{SA}. As expected, greater degradation is observed with increasing N. Some scatter is noted for N = 1 to 3, likely due to extrapolation in the CCD. These curves are conceptual, representing averaged behavior from multiple tests. For reference, the monotonic shear test result is plotted as a black dotted line and shows good agreement with

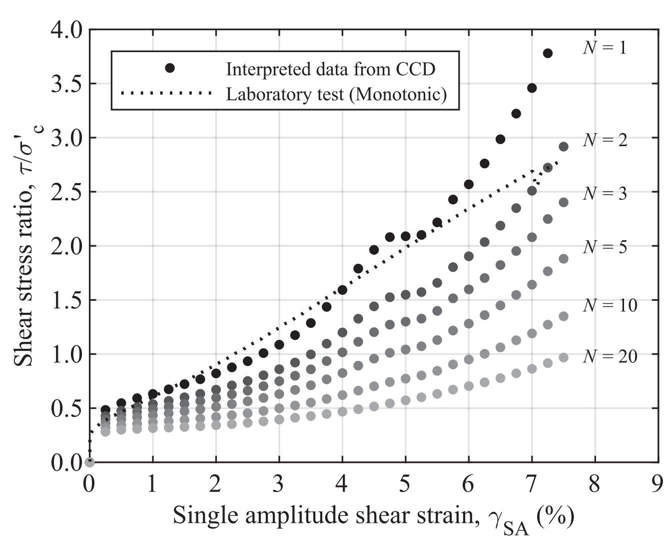

Fig. 18. Degraded shear stress–strain curves for various numbers of cycles interpreted from the CCD.

the curve for $N = 1$, supporting the validity of the approach. In practical design, these degraded curves can be used to calibrate constitutive models for FEA. Alternatively, the stress–strain response can be directly converted into *p–y* curves. Such approaches, known as the mobilizable strength design (MSD) method or the scaling method, have been presented by Bouzid et al. (2013), Lombardi et al. (2017) and Dash et al. (2017) for liquefied soils, and by Zhang et al. (2016) for clay. In either case, an additional step is required to estimate the equivalent number of load cycles N_{eq} from irregular loading histories specific to site conditions. Methods for this estimation are discussed in LeBlanc et al. (2010b), Page et al. (2021) and Lapastoure et al. (2023).

Based on the degraded stress–strain curves (Fig. 18), a degradation factor F_D is introduced as an index of material degradation. Fig. 19 illustrates F_D, defined as the ratio of degraded shear stress to the undegraded shear stress ($N = 1$) for various shear strain levels. For Toyoura sand, a bi-linear trend is observed, with F_D increasing linearly and becoming constant beyond a shear strain of 5%. This behavior aligns with the API modification approach, where cyclic loading primarily affects ultimate strength rather than initial stiffness. To support the following discussion, the degradation factors $F_{D,\min}$ and $F_{D,\max}$ are defined at shear strains of 0% and more than 5%, respectively. In design applications, *p–y* curves can be adjusted using F_D based on the expected deformation level in each design load case, providing a more accurate representation of foundation performance under cyclic loading. To date, it appears more common to apply degradation directly to *p–y* curves rather than to stress–strain curves (e.g., Bouzid et al., 2013; Lapastoure et al., 2025).

4.3. Degradation observed in model tests

To validate the applicability of the CCD concept, the degradation factor F_D was compared with the degree of degradation observed in model test M−3. It is noted that no significant degradation was observed in test S-3 due to the slow loading rate. As an index of degradation in the model tests, the normalized stiffness was evaluated at each cycle of lateral loading, relative to the stiffness in the initial cycle (Fig. 20). Here, stiffness is defined as the secant stiffness between the positive and negative peaks of the load–displacement curves shown in Fig. 4. The results, represented by hollow markers, correspond to monopiles with different slenderness ratios *L*/*D*. A sharp reduction in stiffness was observed after the first few cycles, stabilizing around the 10th cycle. This behavior suggests that the model ground reached a steady-state response under cyclic loading. For the slender monopile ((c) D1.25–*L*10), the normalized stiffness stabilized at approximately 70%. In contrast, the large-diameter monopiles ((a) D2–L7.5 and (b) D2–*L*10) exhibited lower terminal values of around 55%, indicating a greater susceptibility to cyclic degradation. This behavior is attributed to the deformation mechanism associated with large-diameter monopiles, which mobilize a greater volume of surrounding soil, including the region near the pile toe. This increased soil mobilization amplifies the effects of cyclic degradation.

Fig. 20 also presents the range of degradation factors F_D derived from the CCD. The upper and lower boundaries of the range correspond to $F_{D,\max}$ and $F_{D,\min}$, respectively. For $N < 10$, the normalized stiffness values from the model tests mostly fall within the range of F_D predicted by the CCD. Specifically, the results for the slender monopile ((c) D1.25–*L*10) and the large-diameter monopiles ((a) D2–L7.5 and (b) D2–*L*10) closely correspond to the lower and upper bounds of F_D, respectively. Unlike the model tests, however, the CCD-based F_D continues to decrease beyond $N = 10$. This discrepancy may be attributed to differences in drainage conditions. The CCD is based on undrained cyclic shear tests, where pore water pressure accumulates without dissipation, resulting in more pronounced degradation with increasing *N*. In contrast, since

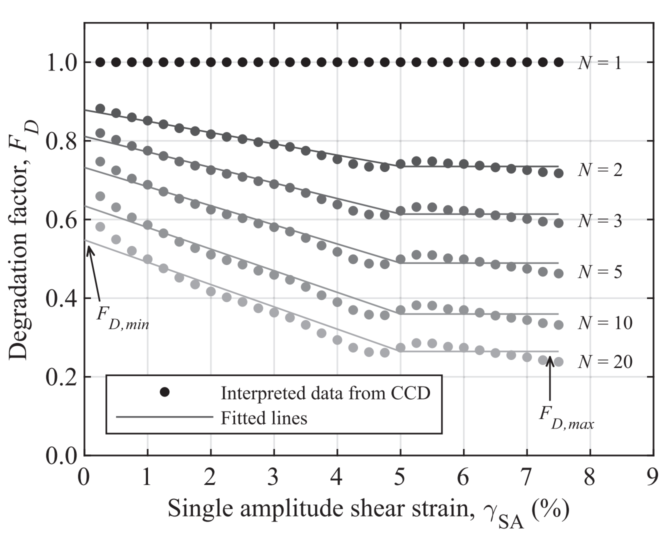

Fig. 19. Degradation factor F_D evaluated at different levels of shear strain.

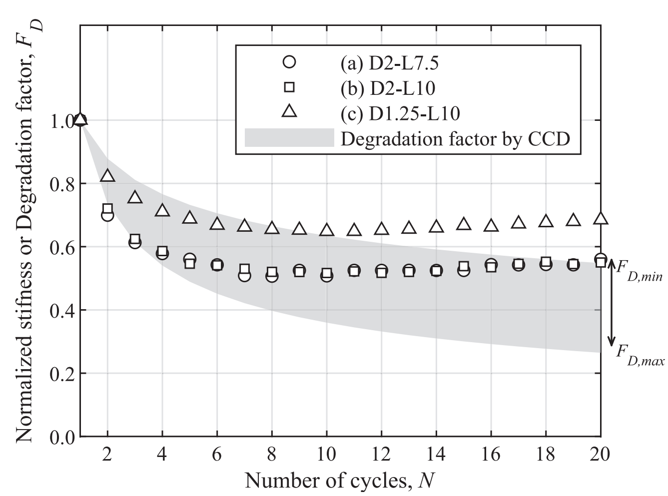

Fig. 20. Normalized stiffness in model test M−3 and degradation factor F_D by CCD.

a steady state was observed during cyclic loading, model test M−3 was likely conducted under partially drained conditions, where a balance between pore water pressure generation and dissipation was achieved. It is also noteworthy that the cyclic loading in the model tests was applied in a deformation-controlled manner. Further reduction may occur under load-controlled loading, which more closely reflects field conditions. A comparison between the model test results and those reported by Tasiopoulou et al. (2025) may provide additional insights into the behavior of monopiles under cyclic loading.

In addition to the discussion above, potential contributing factors include localized densification around the pile due to cyclic shearing in the centrifuge tests. Under loading condition M−3, the effects of excess pore pressure generation, pore pressure dissipation, and soil densification cannot be readily separated based on the available measurements. Therefore, the slower-loading tests (S-3), where excess pore pressure effects are expected to be less significant, were further examined. A slight increase in secant stiffness was observed during the initial loading cycles, suggesting that localized densification may have contributed to the increase in stiffness with increasing cycle number, thereby moderating the apparent degradation. However, changes in density or void ratio were not directly measured in the present study, and a full quantitative separation of these mechanisms is not possible based on the available data.

Here, the drainage conditions in the model tests are further examined. Several studies have focused on analytical solutions for consolidation around a laterally loaded monopile (e.g., Osman and Randolph, 2012; Peralta et al. 2017; Li et al. 2019). In this study, the criterion proposed by Li et al. (2019), a normalized loading factor T_p, was calculated to estimate the drainage conditions in the model tests:

$$T_p = t_p c_v / D^2$$

where t_p is defined as the period of a single loading cycle, i.e. the inverse of the loading frequency, c_v is the coefficient of consolidation, and D is the diameter of the monopile. Following Li et al. (2019), this definition is adopted because drainage during lateral cyclic loading is governed by the time available for pore pressure dissipation within each cycle. Although T_p is defined by a simple expression under idealized conditions, it serves as a practical indicator for distinguishing the drainage condition in the present centrifuge model tests with varying loading periods. Their parametric study based on FE analyses concluded that undrained conditions are expected when $T_p \leq 0.05$. Furthermore, results for $T_p \leq 0.5$ were found to be nearly identical and can also be considered undrained. In contrast, when $T_p > 50$, pore water pressure generation becomes negligible, and the soil can be treated as essentially drained. Table 4 summarizes the calculated T_p values for the model tests at three elevations corresponding to the pore water pressure transducer locations (see Figs. 1 and 15). The values of c_v were estimated from oedometer test results, considering the confining pressure at each sensor location. For loading condition M−3, all calculated T_p values across the monopile models and elevations are below 0.5, indicating undrained conditions. It is important to note that the criterion proposed by Li et al. (2019) is based on FE analyses employing a disc model, which represents a one-meter-thick horizontal slice of the monopile and surrounding soil, where vertical drainage was neglected. As they noted, this assumption is considered reasonable for soil located some distance below the mudline. However, near the mudline, vertical drainage toward the surface may also occur, potentially accelerating the drainage process. Evidence of this vertical drainage effect is also suggested by the results shown in Fig. 16, where excess pore water pressure does not accumulate during cyclic loading at the shallowest measurement point, in contrast to deeper locations. Therefore, the drainage conditions during loading case M−3 were likely to range from nearly undrained to partially drained. Meanwhile, despite the calculated T_p values being less than 50, the drainage conditions during loading case S-3 were likely to be drained, as inferred from the observed pore water pressure behavior.

It is possible to incorporate the effects of partial drainage conditions into the CCD, as demonstrated by Jostad et al. (2015). To achieve this, a CCD based on the excess pore water pressure ratio, rather than shear strain, is required. The dissipation of excess pore water pressure can be analytically estimated, leading to a reduction in the equivalent number of load cycles, N_{eq}. However, this approach relies on a simplified scenario, assuming lateral and radial drainage with a predefined boundary condition of zero excess pore water pressure. Therefore, careful consideration is necessary when applying this method in practical design contexts.

4.4. 3D FEA with degraded parameters

To further assess the applicability of the CCD, additional 3D FEA were performed. The parameters of the HSS model were re-calibrated based on the degradation characteristics derived from the CCD. The re-calibrated parameter sets were then used to simulate the monopile behavior at selected load cycles during loading condition M−3 in the model tests. Fig. 21 presents the simulation results of the DSS test using the re-calibrated parameters (the black solid lines). For the re-calibration, the original simulation result ($N = 1$, the gray solid line) was scaled using the degradation factors F_D corresponding to various numbers of load cycles N (the dashed lines). Among the HSS model parameters, only the initial stiffness G_0^{ref}, friction angle φ' and dilatancy ψ were modified, as summarized in Table 5. It should be noted that the re-calibration does not imply that the intrinsic soil properties physically evolve with the number of loading cycles. Rather, these parameters were treated as cycle-dependent equivalent parameters to reproduce the degraded stress–

Table 4
Normalized loading factor T_p for the model tests S-3 and M−3.

Monopile model	Diameter	Elevation from mudline	Coefficient of consolidation	Normalized loading factor	
	D (m)	$-z$ (m)	c_v (m^2/s)	T_p for S-3 (0.002 Hz)	T_p for M−3 (0.2 Hz)
(a) D2-L7.5	2.0	−2.5	4.38×10^{-2}	5.5	0.05
		−5.0	8.94×10^{-2}	11.2	0.11
		−7.5	1.25×10^{-1}	15.6	0.16
(b) D2-L10	2.0	−2.0	3.30×10^{-2}	4.1	0.04
		−6.0	1.04×10^{-1}	13.0	0.13
		−8.0	1.31×10^{-1}	16.4	0.16
(c) D1.25-L10	1.25	−2.0	3.30×10^{-2}	10.6	0.11
		−6.0	1.04×10^{-1}	33.2	0.33
		−8.0	1.31×10^{-1}	42.1	0.42

strain curves derived from the CCD within the HSS framework. Within the HSS model, G_0^{ref} controls the small-strain stiffness, while φ' and ψ primarily govern the mobilized shear resistance and dilative response at larger strain levels. The values listed in Table 5 should therefore be interpreted as equivalent engineering parameters that capture the effects of cyclic degradation, rather than as directly measurable material properties.

All other conditions of the 3D FEA were kept identical to those described in the former sections. In other words, the FE simulation starts with an intact ground condition, with degradation incorporated solely through the modified model parameters, aiming to replicate monopile behavior under cyclic loading. It should be noted that the approach presented here involves certain simplifications; however, it serves to illustrate both the potential and the limitations of the CCD in practical applications.

Figs. 22–24 present the results of the 3D FEA for $N = 5$, 10, and 20, respectively. The model test results are shown only for the first cycle and the specific cycle of interest. For $N = 5$ (Fig. 22), the FEA yields comparable results; however, the increasing stiffness observed during deformation, particularly in case (b) D2-L10, is not fully captured. This discrepancy is primarily attributed to limitations in the constitutive model. The HSS model utilizes a hyperbolic stress–strain relationship, in which stiffness progressively decreases with increasing deformation. In the FEA, the maximum shear strain remains below 5% in most of the surrounding soil elements, except for those adjacent to the monopile (Fig. 14). Consequently, the dilative behavior observed at shear strains exceeding 5% (Fig. 21) is not fully reflected in the monopile response within the FEA. The methodology adopted in this study, which simply applies the degradation factor F_D to the undegraded curve ($N = 1$), has inherent limitations in accurately reproducing the cyclic behavior of monopiles. Furthermore, in constructing the CCD, only the maximum shear strain observed during each load cycle in the laboratory tests is considered. As a result, the detailed mid-range response is not sufficiently captured. At the load–displacement response level, this effect is explicitly addressed by Erdrich et al. (2010). They distinguished between the initial and subsequent cycle p–y responses for carbonate soils, depending on the load levels experienced in the preceding cycle. The p–y response in the subsequent cycle was modified to include an initial "soft" zone with reduced stiffness, followed by a hardening phase.

When considering only the maximum load levels, better agreement is observed for $N = 10$ (Fig. 23), while the FEA underestimate the model test results for $N = 20$ (Fig. 24). Consistent with the model test results shown in Fig. 20, the normalized stiffness obtained from the FEA is compared with the FD range derived from the CCD, as shown in Fig. 25. In this context, the normalized stiffness from the FEA is defined as the secant stiffness between the origin and the positive peak of the stress–strain curve, normalized by the stiffness of the undegraded curve ($N = 1$). The results, represented by black markers, exhibit a similar reduction trend to the F_D values obtained from the CCD. Furthermore, the large-diameter monopiles are shown to be more susceptible to cyclic degradation, which aligns with the observations from the model tests. As expected, the stiffness continues to decrease up to $N = 20$ in the FEA, unlike the model test results. This finding underscores the importance of accounting for drainage conditions in practical design applications. Another simplification adopted in this study is the assumption of uniform degradation throughout the entire soil volume. In more realistic conditions, the degree of degradation is expected to vary spatially within the surrounding soil. For example, Lapastoure et al. (2025) proposed a method that modifies the p–y curve based on soil mobilization with depth, determined through one-dimensional FEA using beam elements. Such depth-dependent degradation is preferable in practical design for representing more realistic behavior under cyclic loading.

4.5. Implications for practical design

The results of this study provide several insights into the practical application of CCD-based approaches to the

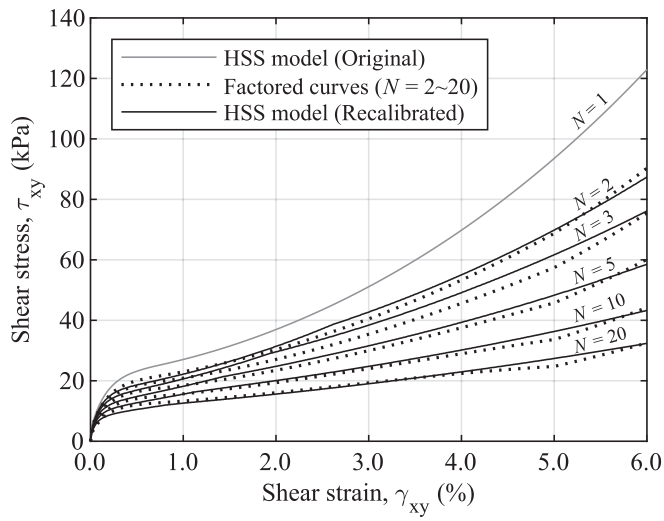

Fig. 21. Recalibration of HSS model, simulation of DSS with degraded parameters.

design of large-diameter monopiles subjected to cyclic lateral loading.

First, the findings highlight the importance of evaluating drainage conditions when applying degradation factors derived from laboratory element tests. As demonstrated in Section 4.3, the cyclic response of monopiles may vary significantly with the extent of pore pressure generation and dissipation during loading. Therefore, the applicability of degradation factors obtained under undrained laboratory conditions should be assessed in conjunction with the expected drainage regime around the monopile. In this regard, the normalized loading factor T_p (Li et al., 2019) may serve as a useful screening indicator for evaluating the expected drainage conditions and the suitability of CCD-derived degradation factors for design assessments.

Second, the numerical analyses indicate that the influence of cyclic degradation is not uniform across monopile geometries. The larger-diameter monopiles exhibited a greater reduction in lateral resistance than the more slender monopiles, suggesting that cyclic degradation may have a stronger impact on monopiles that rely significantly on rotational resistance and base resistance. This observation emphasizes the need to consider pile geometry when interpreting degradation factors for design purposes.

Third, the comparison between the centrifuge tests and the 3D FE analyses suggests that CCD-derived degradation factors can be incorporated into finite-element-based design assessments by re-calibrating constitutive model parameters.

Overall, the present results demonstrate that the practical use of CCD-based degradation factors requires consideration of drainage conditions, pile geometry, and the governing deformation mechanisms around the monopile. Careful interpretation of these factors is essential when applying laboratory-derived degradation relationships to the design of offshore monopile foundations.

5. Conclusions

The key conclusions derived from this study are as follows.

- The HSS model demonstrates good predictive capability for the behavior of saturated dense sand when parameters are carefully calibrated using laboratory test data. The 3D FEA effectively captures the monotonic loading response of monopiles with varying slenderness ratios ($L/D = 3.75$, 5 and 8) under loading conditions ranging from fully drained to partially drained and nearly undrained.
- The CCD and degradation factor F_D were evaluated based on the results from undrained hollow cylinder cyclic torsional shear tests as an alternative to DSS. A bilinear trend is observed for F_D of Toyoura sand, with F_D becoming constant beyond a shear strain of 5%. This behavior aligns with the conventional API modification approach, where cyclic loading primarily affects ultimate strength rather than initial stiffness.
- To validate the applicability of the CCD concept, the degradation factor F_D was compared with the result of model test M−3. Unlike the model tests, the CCD-based F_D continues to decrease beyond $N = 10$. This discrepancy may be attributed to differences in drainage conditions. The CCD is based on undrained cyclic shear tests, where pore water pressure accumulates without dissipation, resulting in more pronounced degradation with increasing N. In contrast, model test M−3 was likely conducted under partially drained conditions as evidenced by a steady state observed during cyclic loading and the criterion proposed by Li et al. (2019). These findings highlight the importance of evaluating drainage conditions when applying CCD-derived degradation

Table 5
Parameters of HSS model for various levels of degradation.

Parameter		Unit	$N = 1$	$N = 2$	$N = 3$	$N = 5$	$N = 10$	$N = 20$
Reference shear modulus at small strain	G_0^{ref}	kN/m^2	5.000×10^4	4.392×10^4	4.057×10^4	3.661×10^4	3.174×10^4	2.740×10^4
Threshold shear strain at 70% of G_0	$\gamma_{0.7}$	–	0.15×10^{-3}	0.15×10^{-3}	0.15×10^{-3}	0.15×10^{-3}	0.15×10^{-3}	0.15×10^{-3}
(Effective) cohesion	c'_{ref}	kN/m^2	0.0	0.0	0.0	0.0	0.0	0.0
(Effective) angle of internal friction	φ'	degree	40.0	32.0	28.0	23.0	18.5	14.0
Angle of dilatancy	ψ	degree	10.0	8.0	7.5	6.5	5.5	5.0

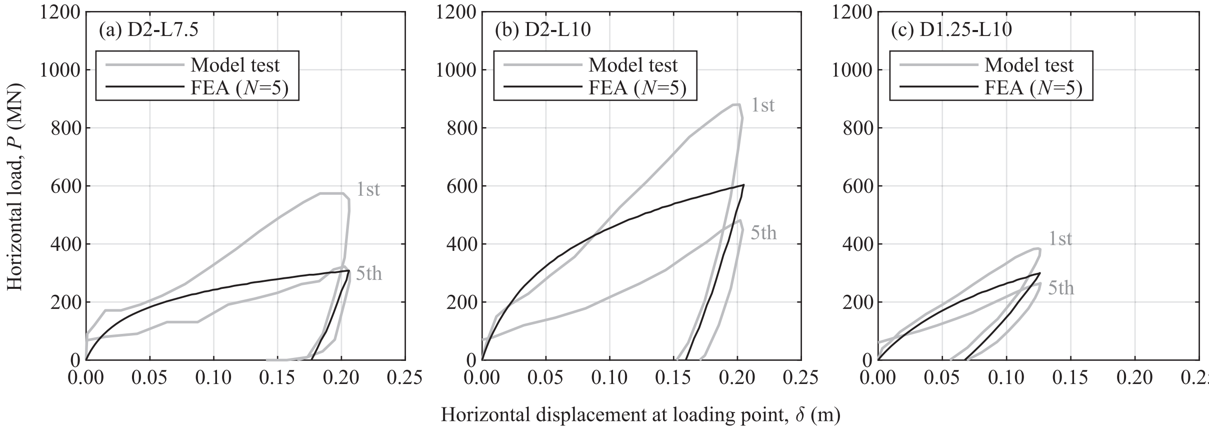

Fig. 22. Simulation of model test M−3 with degraded parameters for $N = 5$: Load-displacement response at loading point.

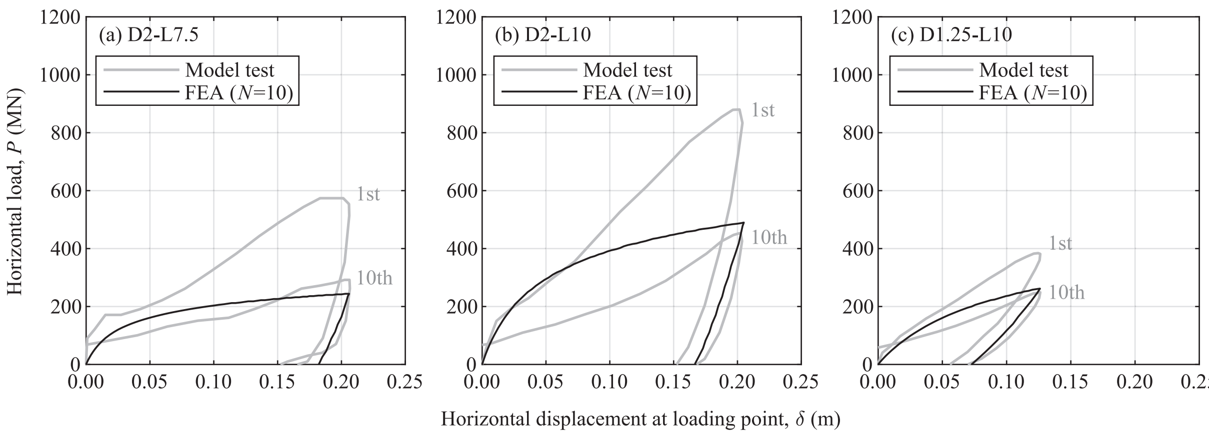

Fig. 23. Simulation of model test M−3 with degraded parameters for $N = 10$: Load-displacement response at loading point.

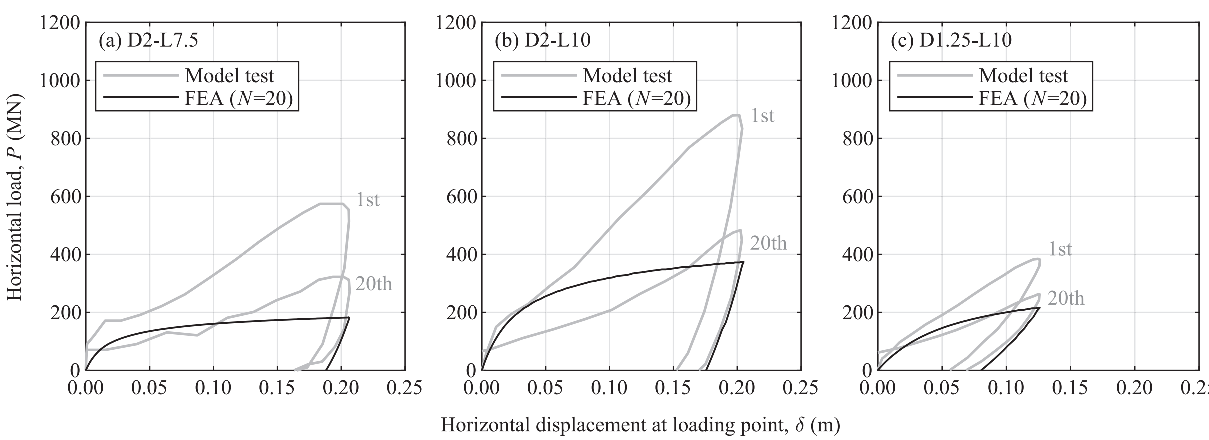

Fig. 24. Simulation of model test M−3 with degraded parameters for $N = 20$: Load-displacement response at loading point.

factors to monopile design. The normalized loading factor T_p may provide a useful screening indicator for assessing the expected drainage regime and the suitability of CCD-based approaches.

- Additional 3D FEA were performed to further assess the applicability of the CCD. The parameters of the HSS model were recalibrated based on the degradation characteristics derived from the CCD. The FEA yields comparable results; however, the increasing stiffness observed during deformation, particularly in case (b) D2-*L*10, is not fully captured. A clear distinction between primary and subsequent loading cycles is necessary to accurately reproduce the cyclic behavior of monopiles, as highlighted by Erdrich et al. (2010) in their modification of the p–y curve.

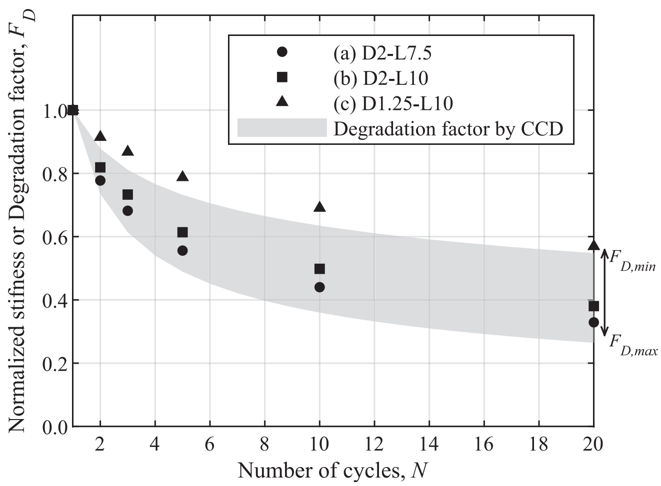

Fig. 25. Normalized stiffness by 3D FEA using degraded parameters and degradation factor F_D by CCD.

- When considering only the maximum load levels, better agreement is observed between the model test and the FEA using degraded parameters. The FEA exhibits a similar reduction trend to the F_D values obtained from the CCD. Furthermore, the large-diameter monopiles are shown to be more susceptible to cyclic degradation, which aligns with the observations from the model tests. This observation suggests that pile geometry plays an important role in governing the influence of cyclic degradation and should therefore be considered when interpreting degradation factors for practical design applications.
- The novelty of this study does not lie in the development of a new constitutive model or a new finite element formulation. Rather, it lies in translating CCD-derived element-level degradation into pile-level design interpretations for large-diameter monopiles by integrating cyclic laboratory testing, CCD-based degradation assessment, and three-dimensional finite element analysis. The results demonstrate that the practical application of CCD-based approaches requires consideration of drainage conditions, pile geometry, and the governing deformation mechanisms around the monopile. The present study provides insight into how laboratory-derived cyclic degradation characteristics can be incorporated into finite-element-based assessments of large-diameter monopiles.

CRediT authorship contribution statement

Takaaki Kobayashi: . **Jaylord Tan Tian:** Writing – review & editing, Investigation, Data curation. **Shintaro Ohno:** Writing – review & editing, Validation, Methodology. **Toshihiro Sawada:** Visualization, Validation, Investigation. **Akihiro Takahashi:** Writing – review & editing, Validation, Supervision, Methodology, Formal analysis.

Declaration of Generative AI and AI-assisted technologies in the writing process

During the preparation of this work, the authors used Microsoft Copilot in order to improve the readability of the manuscript. After using this tool, the authors reviewed and edited the content as needed and take full responsibility for the content of the publication.

Acknowledgements

The authors are grateful to Kawasaki Geological Engineering Company for their excellent work on soil testing and helpful discussions. The authors are indebted to Mr. Sakae Seki, a technician at the Tokyo Institute of Technology, for his continuous cooperation in the centrifuge experiments.

References

API (American Petroleum Institute), 2000. Recommended Practice for Planning, Designing and Constructing Fixed Offshore Platforms-Working Stress Design, RP 2A-WSD, 21st Ed., Washington, DC, USA.

Andersen, K. H., 2015. Cyclic soil parameters for offshore foundation design. The Third ISSMGE McClelland Lecturer, Frontiers in Offshore Geotechnics III.

Bentley Systems, 2023a. PLAXIS 3D Reference Manual 3D (Version 2024.1).

Bentley Systems, 2023b. PLAXIS 3D Material Models Manual 3D (Version 2024.1), 67-93.

Bentley Systems, 2023c. PLAXIS Monopile Designer Manual, 117-121.

Benz, T., 2007. Small-Strain Stiffness of Soils and It's Numerical Consequences. University of Stuttgart, Institute of Geotechnical Engineering, Stuttgart, Germany, PhD Thesis.

Bouzid, D.A., Bhattacharya, S., Dash, S.R., 2013. Winkler springs (p-y curves) for pile design from stress-strain of soils: FE assessment of scaling coefficients using the mobilized strength design concept. Geomech. Eng. 5 (5), 379–399.

Brinkgreve, R., Lisi, D., Lahoz, M., Panagoulias, S., 2020. Validation and application of a new software tool implementing the PISA design methodology. J. Marine Sci. Eng. 8, 457.

Burd, H.J., Taborda, D.M.G., Zdravković, L., Abadie, C.N., Byrne, B. W., Houlsby, G.T., Gavin, K.G., Igoe, D.J.P., Jardine, R.J., Martin, C.M., McAdam, R.A., Pedro, A.M.G., Potts, D.M., 2020. PISA design model for monopiles for offshore wind turbines: application to a marine sand. Géotechnique 70 (11), 1048–1066.

Byrne, B.W., Burd, H.J., Houlsby, G.T., Kamas, I., Keane, R., Malhotra, S., Martin, S.C., Nardelli, V., Qiu, Z., Rasmussen, M.E., Simonin, L., Saberi, M., Wen, K.Z., Wu, K.-K., Buckley, R., Crispin, J.J., Shonberg, A., Soares Cunha, V., Vaitkune, E., 2025. PICASO: Cyclic loading of wind turbine monopiles. Proceedings of the 5th International Symposium on Frontiers in Offshore Geotechnics (ISFOG 2025), Nantes, France.

Chaloulos, Y.K., Tasiopoulou, P., Giannakou, A., Chacko, J., Aghakouchak, A., Stergiou, T., 2024. Fully-coupled cyclic time-history analyses of monopile foundations in sand. Ocean Eng. 298 116691.

Dash, S.R., Rouholamin, M., Bhattacharya, S., 2017. A practical method for construction of p-y curves for liquefiable soils. Soil Dyn. Earthq. Eng. 97, 478–481.

DNV-RP-C212, 2021. Offshore soil mechanics and geotechnical engineering, DNV, Høvik, Norway.

Erdrich, C.T., O'Neill, M.P., Clancy, P., Randolph, M.F., 2010. Axial and lateral pile design in carbonate soils. Proc. 2nd International Symposium on Frontiers in Offshore Geotechnics, pp. 125–154.

Ishii, Y., Shimada, K., Ishihara, T., 2024. Finite Element Analysis of Lateral Soil Reaction of Monopile in Sand Considering Effects of Pile Installation Process. In: The 34th International Ocean and Polar Engineering Conference, ISOPE, 2024.

JGS, 2015. JAPANESE GEOTECHNICAL SOCIETY STANDARDS Laboratory Testing Standards of Geomaterials (Vol. 1), JGS 0411 Test method for one-dimensional consolidation properties of soils using incremental loading (JIS A1217).

JGS, 2017a. JAPANESE GEOTECHNICAL SOCIETY STANDARDS Laboratory Testing Standards of Geomaterials (Vol. 2), JGS 0542 Method for cyclic triaial test to determine deformation properties of geomaterials.

JGS, 2017b. JAPANESE GEOTECHNICAL SOCIETY STANDARDS Laboratory Testing Standards of Geomaterials (Vol. 2), JGS 0541 Method for cyclic undrained triaxial test on soils.

JGS, 2018. JAPANESE GEOTECHNICAL SOCIETY STANDARDS Laboratory Testing Standards of Geomaterials (Vol.3), JGS 0551 Method for torsional shear test on hollow cylindrical specimens of soils.

Jostad, H.P., Grimstad, G., Andersen, K.H., Sivasithamparam, H., 2015. A FE procedure for calculation of cyclic behaviour of offshore foundations under partly drained conditions. Front. Off. Geotech. III 1, 153–172.

Jostad, H.P., Dahl, B.M., Page, A., Sivasithamparam, N., Sturm, H., 2020. Evaluation of soil models for improved design of offshore wind turbine foundations in dense sand. Geotechnique 70 (8), 682–699.

Kaltekis, K., Whyte, S., Vahdatirad, M. J., Abyaneh, S., Burbury, D., Mclean, R., Francis, M., Hilton, J., Berberi, S., 2023. A review of constitutive models for an FEA-based monopile design. In: Offshore Site Investigation and Geotechnics 9th International Conference Proceeding. pp. 1614–1621.

Lapastoure, L.M., Diambra, A., Jalilvand, S., Igoe, D., 2023. Assessment of cyclic superposition approaches for the cyclic design of monopiles supporting offshore wind turbines. Ocean Eng. 287 115759.

Lapastoure, L.M., Jalilvand, S., Igoe, D., 2025. Validation of a contour diagram-based model for monopile cyclic design in sand and clay. Acta Geotech., 1–15

LeBlanc, C., Houlsby, G.T., Byrne, B.W., 2010a. Response of stiff piles in sand to long-term cyclic lateral loading. Geotechnique 60 (2), 79–90.

LeBlanc, C., Byrne, B.W., Houlsby, G.T., 2010b. Response of stiff piles to random two-way lateral loading. Geotechnique 60 (9), 715–721.

Li, S., Zhang, Y., Jostad, H.P., 2019. Drainage conditions around monopiles in sand. Appl. Ocean Res. 86, 111–116.

Liu, H., Kaynia, A.M., 2022. Monopile responses to monotonic and cyclic loading in undrained sand using 3D FE with SANISAND-MSu. Water Sci. Eng. 15 (1), 69–77.

Liu, H., Kementzetzidis, E., Abell, J.A., Pisanò, F., 2022. From cyclic sand ratcheting to tilt accumulation of offshore monopiles: 3D FE modelling using SANISAND-MS. Géotechnique 72 (9), 753–768.

Lombardi, D., Dash, S.R., Bhattacharya, S., Ibraim, E., Muir Wood, D., Taylor, C.A., 2017. Construction of simplified design p–y curves for liquefied soils. Géotechnique 67 (3), 216–227.

McAdam, R.A., Byrne, B.W., Houlsby, G.T., Beuckelaers, W.J.A.P., Burd, H.J., Gavin, K.G., Igoe, D.J.P., Jardine, R.J., Martin, C.M., Muir Wood, A., Potts, D.M., Gretlund, J.S., Taborda, D.M.G., Zdravković, L., 2020. Monotonic laterally loaded pile testing in a dense marine sand at Dunkirk. Géotechnique 70 (11), 986–998.

Osman, A.S., Randolph, M.F., 2012. Analytical solution for the consolidation around a laterally loaded pile. Int. J. Geomech. 12 (3), 199–208.

Page, A.M., Klinkvort, R.T., Bayton, S., Zhang, Y., Jostad, H.P., 2021. A procedure for predicting the permanent rotation of monopiles in sand supporting offshore wind turbines. Mar. Struct. 75 102813.

Peralta, P., Ballard, J. C., Rattely, M., Erdrich C. E., 2017. Dynamic and cyclic pile-soil response curves for monopile design. In: Offshore Site Investigation and Geotechnics 9th International Conference Proceeding, Smarter Solutions for Future Offshore Developments. pp. 1054–1061.

Pisanò, F., 2019. Input of advanced geotechnical modelling to the design of offshore wind turbine foundations. Proceedings of the XVII ECSMGE-2019: Geotechnical Engineering Foundation of the Future, pp. 1–6.

Pisanò, F., Kementzetzidis, E., Wang, H., Marino, M., Zwaan, R., Peccin da Silva, A., Konstadinou, M., Elkadi, A., Liu, H., Askarinejad, A., Jostad, H.P., 2025. Proceedings of the 5th International Symposium on Frontiers in Offshore Geotechnics (ISFOG 2025), Nantes, France.

Schanz, T., Vermeer, P.A., Bonnier, P.G., 1999. The hardening soil model: formulation and verification. Beyond 2000 in Computational Geotechnics, pp. 281–296.

Taborda, D.M.G., Zdravković, L., Potts, D.M., Burd, H.J., Byrne, B.W., Gavin, K.G., Houlsby, G.T., Jardine, R.J., Liu, T., Martin, C.M., McAdam, R.A., 2020. Finite-element modelling of laterally loaded piles in a dense marine sand at Dunkirk. Géotechnique 70 (11), 1014–1029.

Takahashi, A., Omura, N., Kobayashi, T., Kamata, Y., Inagaki, S., 2022. Centrifuge model tests on large-diameter monopiles in dense sand subjected to two-way lateral cyclic loading in short-term. Soils Found. 62 (3) 101148.

Tantivangphaisal, P., Taborda, D.M.G., Kontoe, S., 2024. Numerical modelling of the long-term cyclic ratcheting of monopile foundations under lateral loading. Proceedings of the XVIII European Conference on Soil Mechanics and Geotechnical Engineering, pp. 3349–3352.

Tasiopoulou, P., Limnaiou, T., Sakellariadis, L., Chacko, J., Jones, L.A., Agalianos, A., Anastasopoulos, I., 2025. Centrifuge modelling of an OWT monopile foundation in saturated sand subjected to cyclic dynamic storm loading. Proceedings of the 5th International Symposium on Frontiers in Offshore Geotechnics (ISFOG 2025), Nantes, France.

Zhang, Y., Andersen, K.H., Klinkvort, R.T., Jostad, H.P., Sivasithamparam, N., Boylan, Noel, P., Langford, T., 2016. Monotonic and cyclic p-y curves for clay based on soil performance observed in laboratory element tests. Offshore Technology Conference OTC-29642-MS.